Received: 1 July 2022 | Revised: 6 October 2022 | Accepted: 25 October 2022 | Published on: 13 November 2022

DOI: 10.1002/mrm.29524

RESEARCH ARTICLE

Magnetic Resonance in Medicine

B_1^+-correction of magnetization transfer saturation maps optimized for 7T postmortem MRI of the brain

Ilona Lipp[1] | Evgeniya Kirilina[1] | Luke J. Edwards[1] | Kerrin J. Pine[1] | Carsten Jäger[1,2] | Tobias Gräßle[3] | EBC Consortium[1] | Nikolaus Weiskopf[1,4] | Gunther Helms[1,5]

[1]Department of Neurophysics, Max Planck Institute for Human Cognitive and Brain Sciences, Leipzig, Germany

[2]Paul Flechsig Institute of Brain Research, Medical Faculty, Leipzig University, Leipzig, Germany

[3]Epidemiology of Highly Pathogenic Microorganisms, Robert Koch-Institute, Berlin, Germany

[4]Felix Bloch Institute for Solid State Physics, Faculty of Physics and Earth Sciences, Leipzig University, Leipzig, Germany

[5]Department of Clinical Sciences and Medical Radiation Physics, Lunds Universitet, Lund, Sweden

Correspondence
Ilona Lipp, Department of Neurophysics, Max Planck Institute for Human Cognitive and Brain Sciences, Stephanstr. 1a, 04103 Leipzig, Germany.
Email: lippi@cbs.mpg.de

Funding information
Deutsche Forschungsgemeinschaft, Grant/Award Numbers: 347592254 (WE5046/4-2,KI1337/2-2), 446291874; Horizon 2020 Framework Programme, Grant/Award Number: 681094; Seventh Framework Programme, Grant/Award Number: 616905; Vetenskapsrådet, Grant/Award Number: NT 2014-6193

Purpose: Magnetization transfer saturation (MTsat) is a useful marker to probe tissue macromolecular content and myelination in the brain. The increased B_1^+-inhomogeneity at ≥ 7 T and significantly larger saturation pulse flip angles which are often used for postmortem studies exceed the limits where previous MTsat B_1^+ correction methods are applicable. Here, we develop a calibration-based correction model and procedure, and validate and evaluate it in postmortem 7T data of whole chimpanzee brains.

Theory: The B_1^+ dependence of MTsat was investigated by varying the off-resonance saturation pulse flip angle. For the range of saturation pulse flip angles applied in typical experiments on postmortem tissue, the dependence was close to linear. A linear model with a single calibration constant C is proposed to correct bias in MTsat by mapping it to the reference value of the saturation pulse flip angle.

Methods: C was estimated voxel-wise in five postmortem chimpanzee brains. "Individual-based global parameters" were obtained by calculating the mean C within individual specimen brains and "group-based global parameters" by calculating the means of the individual-based global parameters across the five brains.

Results: The linear calibration model described the data well, though C was not entirely independent of the underlying tissue and B_1^+. Individual-based correction parameters and a group-based global correction parameter ($C = 1.2$) led to visible, quantifiable reductions of B_1^+-biases in high-resolution MTsat maps.

Conclusion: The presented model and calibration approach effectively corrects for B_1^+ inhomogeneities in postmortem 7T data.

KEYWORDS

calibration, chimpanzee, magnetization transfer, MRI, postmortem, transmit field, ultra high-field

1 | INTRODUCTION

Quantitative MRI (qMRI) is a powerful tool to study brain anatomy.[1] qMRI parameters in the brain provide measures of tissue myelination, and can be compared between in vivo and postmortem, across brain regions, across individuals, and even across species, opening the door for a plethora of neuroscience applications.[1-6] In the postmortem brain, ultra-high field, ultra-high resolution qMRI facilitates studies of white matter myelination and cortical myeloarchitecture across the whole brain with resolutions down to tens of microns.[7,8]

Magnetization transfer (MT) is a contrast mechanism which is particularly specific to brain myelin. The extended lipid–water interface of myelin facilitates efficient MT between the MRI-visible water protons (the free water pool) and the MRI-invisible protons of macromolecules (the macromolecular pool).[9,10] MT imaging exploits the broad absorption line of macromolecular pool protons.[1,9] The broad line allows selective saturation of the macromolecular pool by off-resonance radiofrequency (RF) pulses applied at a frequency remote from the narrow resonance line of the free water (so-called MT pulses). Subsequent transfer of magnetization between the two pools results in a detectable reduction of the measured free water MRI signal.[11]

Various acquisition schemes for MT quantification have been developed, which differ in complexity, speed, precision, and accuracy.[9,10,12,13] One time-efficient approach is multiparameter mapping (MPM) to acquire maps of the MT saturation (MTsat).[13,14] The MPM approach consists of three RF-spoiled three-dimensional (3D) Fast Low Angle SHot (FLASH) acquisitions and provides a high signal-to-noise ratio (SNR);[13,15,16] it is therefore particularly suitable for ultra-high resolution qMRI on postmortem brains. MTsat values are dependent on the properties of the MT saturation pulse. MTsat cannot, therefore, be strictly considered as a physical parameter of the spin system within the tissue (unlike, e.g., relaxation rates, which are ideally independent of the acquisition method). However, if identical experimental conditions are achieved across the entire brains and between acquisitions (e.g. by using parallel transmit-based approaches[17]), MTsat provides semi-quantitative maps, proportional to the tissue macromolecular pool fraction. Alternatively, MTsat values can be corrected for their dependence on the MT saturation pulse properties (such as shape, length, and amplitude).

While ultra-high field offers advantages with respect to signal-to-noise ratio and is therefore a method of choice for ultra-high resolution imaging, it poses particular challenges for quantitative MT mapping. Increased inhomogeneity of the RF transmit field (B_1^+) at ultra-high field[18,19] results in a spatially varying saturation efficiency of the macromolecular pool which is reflected in a spatial variation in the MT estimates which needs to be corrected for.[13,20-22] The simple correction scheme proposed for in vivo 3T imaging, where the B_1^+ dependency in MTsat is effectively removed by dividing the maps by $(B_1^+)^2$,[13] does not work for the high-power MT pulses which are used in ultra-high resolution postmortem imaging. In vivo work at 3T and 7T demonstrated a correction for B_1^+-dependency on MTsat based on empirical calibration of the MTsat values.[21,23,24] Here we extend this empirical approach for MT pulses with even higher power for application in postmortem MTsat imaging.

To achieve an effective correction, below we empirically determine the dependence of MTsat on B_1^+ in a calibration experiment on postmortem chimpanzee brains. We demonstrate that a simple linear model using only one calibration parameter is sufficient to accurately correct the data. Our correction approach also allows for harmonizing across protocols that apply MT pulses with different flip angles. Thus, it can correct not only for spatial inhomogeneities in B_1^+ but also account for different imaging protocols or scanner hardware modifications.

2 | THEORY

2.1 | Definition of MTsat

In the MT-weighted acquisition in the MPM acquisition scheme a strong off-resonance MT saturation pulse applied every repetition time (TR) causes selective saturation of the macromolecular pool, which is then transferred to the free water pool (Figure 1).[11] The MTsat is defined as the percentage difference in the free water pool magnetization over one TR period (Figure 1B) relative to the magnetization at the beginning of the TR,[13] and is an indirect measure of tissue macromolecular content, m[25] [1]. MTsat is usually reported in percent units (p.u.).

2.2 | Estimation of MTsat

MTsat is estimated using three 3D FLASH acquisitions with different weightings (see Figure 1): (i) an MT-weighted acquisition (S_{MT}) using a small on-resonance flip angle α_{MT} and an off-resonance MT pulse with nominal flip angle β_{nom} which selectively

[1]MTsat differs from the commonly used MT ratio (MTR)[12] in that it is inherently corrected for TR and on-resonance excitation flip angle dependence.[13,26]

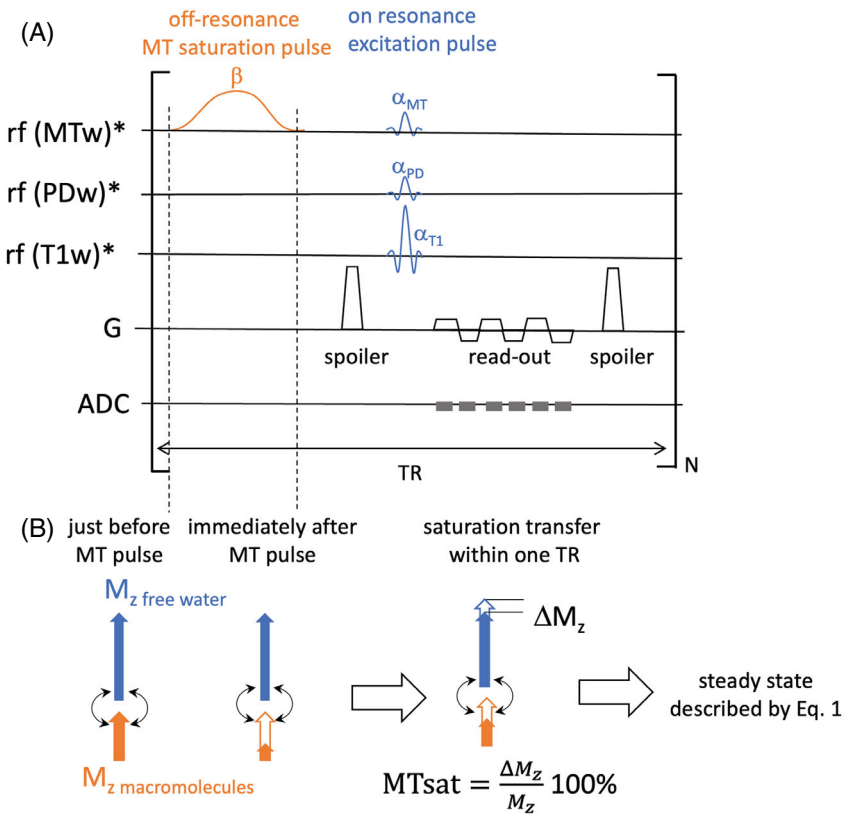

FIGURE 1 (A) Schematic representation of the multiparameter mapping pulse sequence for estimation of magnetization transfer saturation (MTsat), consisting of three 3D Fast Low Angle SHot acquisitions, each with a different radiofrequency (RF) excitation scheme (three upper rows). The MT-weighted acquisition uses a low-flip angle on-resonance excitation pulse with flip angle α_{MT}, and an off-resonance MT pulse with flip angle β_{nom} which selectively saturates the macromolecular pool. The proton density-weighted and T1-weighted acquisitions use low-flip angle (α_{PD}) and large-flip angle (α_{T1}) on-resonance pulses, respectively. Here we assume repetition time (TR) is the same for all acquisitions. (B) MTsat is defined as the difference in the free water magnetization due to the MT pulse over one TR, expressed in percent units of the free water pool magnetization. MTsat results from the exchange of magnetization between the macromolecular pool, which is selectively saturated by the MT pulse, and the free water pool and is dependent on macromolecular tissue content and the degree of saturation of the macromolecular pool.

saturates the macromolecular pool, (ii) a proton density (PD)-weighted acquisition (S_{PD}) using a small on-resonance flip angle α_{PD}, and (iii) a T1-weighted acquisition (S_{T1}) using a large on-resonance flip angle α_{T1}. Assuming MTsat, α_{MT} and R1 · TR are all small, MTsat can be estimated using:[13,14]

$$\mathrm{MTsat} = \left(\frac{S_0\alpha_{MT}}{S_{MT}} - 1\right)\mathrm{R1TR} - \frac{(\alpha_{MT})^2}{2}, \tag{1}$$

where S_0 is the equilibrium magnetization (proportional to PD) and R1 is the longitudinal relaxation rate. We estimate S_0 and R1 using solutions of an exact algebraization of the Ernst equation[2]:[27]

$$S_0 = \frac{S_{PD}S_{T1}}{2}\frac{[\tan(\alpha_{T1}/2)/\tan(\alpha_{PD}/2)] - [\tan(\alpha_{PD}/2)/\tan(\alpha_{T1}/2)]}{S_{T1}\tan(\alpha_{T1}/2) - S_{PD}\tan(\alpha_{PD}/2)}, \tag{2}$$

and

$$\mathrm{R1} = \frac{2}{\mathrm{TR}}\tanh^{-1}\left(\frac{S_{T1}\tan(\alpha_{T1}/2) - S_{PD}\tan(\alpha_{PD}/2)}{[S_{PD}/\tan(\alpha_{PD}/2)] - [S_{T1}/\tan(\alpha_{T1}/2)]}\right). \tag{3}$$

[2]This method of computing S_0 and R1 differs from that in Reference 13, which made use of small angle approximations with respect to α_{PD} and α_{T1} to simplify the calculation. We avoid relying on the small angle approximation here because large α_{T1} are often used in postmortem high resolution imaging to impose sufficient T1-weighting (e.g., in our case $\alpha_{T1} = 84°$).

2.3 | B_1^+ bias in MTsat

Inhomogeneiety of the transmit RF magnetic field B_1^+ results in spatial variation of the flip angles (α_{PD}, α_{T1}, α_{MT} and β_{nom}) across the imaged object such that locally the flip angles are $f_T\alpha_{PD}$, $f_T\alpha_{T1}$, $f_T\alpha_{MT}$, and $f_T\beta_{nom}$, where f_T is the dimensionless local relative bias in B_1^+ which is determined in a separate calibration experiment.[28,29] For convenience in the following we define

$$\beta_{loc} = f_T\beta_{nom}, \tag{4}$$

where subscript "loc" denotes the "local" flip angle.

Equations (1), (2), and (3) can be be modified to account for the spatial variation of the on-resonance excitation flip angles by substituting $f_T\alpha_{PD}$, $f_T\alpha_{T1}$, and $f_T\alpha_{MT}$ for the respective nominal flip angles. However, Equation (1) contains an implicit dependence on β_{loc} which has not been accounted for: the spatial variation in β_{loc} will result in a spatial variation in the saturation of the macromolecular pool, which will result in a spatial variation of the computed MTsat.

MTsat is thus modulated by two factors: the local macromolecular pool fraction, m, and the local MT pulse flip angle, β_{loc}.[13] While the dependence of MTsat on m is an effect of interest used for myelin quantification, its dependence on β_{loc} and therefore on B_1^+ leads to a

spatially dependent bias in MTsat maps which needs to be corrected for to enable accurate whole-brain myelin mapping. Here we present a correction method which aims to render the estimated MT saturation values insensitive to spatial B_1^+ inhomogeneities for postmortem brain imaging at 7T, where formaldehyde-fixed tissue and MT saturation pulses with high power are used.

2.4 | Dependence of MTsat on the MT flip angle

2.4.1 | Model assumptions and plausibility arguments

We assume [3] that the dependence of MTsat on m and β_{loc} can be simply factorized into the product:[11]

$$\text{MTsat}(m, \beta_{\text{loc}}) = \zeta(m)\varphi(\beta_{\text{loc}}). \tag{5}$$

The plausibility of this assumption will be tested experimentally in Section 4. In the following we leave the dependence of MTsat on m implicit.

To correct for the effect of B_1^+ inhomogeneity on MTsat we need to determine the function $\varphi(\beta_{\text{loc}})$.

Physical considerations reveal that $\varphi(\beta_{\text{loc}})$ must have a sigmoidal dependence on β_{loc} (Figure 2A). At low β_{loc}, MTsat has a quadratic dependence due to the differential absorption law of the macromolecular pool.[9] On the other hand, it approaches a limiting value at very high β_{loc} as the macromolecular pool becomes fully saturated after every MT pulse. However, the exact functional form of $\varphi(\beta_{\text{loc}})$ is in general unknown and is dependent on experimental conditions (magnetic field strength, MT pulse parameters) and characteristics of the investigated tissue (fixation method, temperature).

To provide a correction of MTsat for a particular experiment we must find a model of the functional form of $\text{MTsat}(\beta_{\text{loc}})$ for the given experimental conditions over the range of β_{loc} observed in the experiment, which we can then use to correct MTsat to a reference MT flip angle, β_{ref}[4].

Here we develop an empirical approach to obtain a correction for the imaging of postmortem brains at ultra-high fields. This approach is particularly useful for large brains (such as humans, apes, whales, elephants) where the size of the brain is comparable with the electromagnetic field wavelength and therefore the inhomogeneity of B_1^+ field across the brain is particularly strong. The essence of this approach is to make repeated measurements at a range of β_{loc} by scaling β_{nom} to obtain a set of $\text{MTsat}(\beta_{\text{loc}})$ for each voxel.[21,24] These measured data can then be combined to elucidate the β_{loc} dependence and derive a correction for it. While we examine the specific case of chimpanzee brains at 7T here, the general empirical approach could be applied to derive a correction model for any case.

2.5 | Linear model of the dependence of MTsat on the MT flip angle

Figure 2B shows the empirical dependence of MTsat on β_{loc} measured in two distinct regions of a postmortem formalin fixed chimpanzee brain. The shaded area gives the range of β_{loc} values typically used in postmortem experiments. It can be seen that MTsat is empirically linear over the acquired range of β_{loc} for both a gray matter (low myelin) and a white matter (high myelin) region. The linear dependence of β_{loc} suggests that we are in a linear transition region between the quadratic regime and the saturated regime (Figure 2A). We thus propose a linear functional form for the dependence of MTsat on β_{loc}:

$$\varphi(\beta_{\text{loc}}) = 1 + (\beta_{\text{loc}} - \beta_{\text{ref}})A, \tag{6}$$

where A is a coefficient independent of m and β_{loc}, and β_{ref} is the reference MT saturation flip angle we want to map MTsat to. Here we have used the fact that the function $\varphi(\beta_{\text{loc}})$ is defined up to a multiplicative factor to define φ such that $\varphi(\beta_{\text{ref}}) = 1$. Under these assumptions, Equation (5) can be rewritten as:

$$\text{MTsat}(\beta_{\text{loc}}) = (1 + (\beta_{\text{loc}} - \beta_{\text{ref}})A)\text{MTsat}(\beta_{\text{ref}}), \tag{7}$$

where $\text{MTsat}(\beta_{\text{ref}})$ is the corrected MT saturation at β_{ref}. The assumed multiplicative dependence on $\zeta(m)$ (see Equation 5) enters this equation through $\text{MTsat}(\beta_{\text{ref}})$. This model can also be regarded as the first order Taylor series approximation of $\text{MTsat}(\beta_{\text{loc}})$ with respect to β_{loc} around β_{ref}, with $\text{MTsat}(\beta_{\text{ref}})$ the constant term and $A\text{MTsat}(\beta_{\text{ref}})$ the linear term.

The model parameter A can be estimated from the experimental data by voxel-wise linear regression of Equation (7) using $\text{MTsat}(\beta_{\text{loc}})$ as the dependent variable and $(\beta_{\text{loc}} - \beta_{\text{ref}})$ as the independent variable. $\text{MTsat}(\beta_{\text{ref}})$ is then given by the intercept of the linear model, while the parameter A is given by the slope divided by the intercept of the model.

[3]We implicitly exclude potential contributions from direct saturation of the free pool by the MT pulse,[11] which would scale with β_{loc} but not with m. Both Bloch simulations of the direct saturation and fitting the experimental data with a model including a MTsat-independent term (data not shown), suggest that the direct saturation contribution is negligible (< 0.5 p.u.) for our off-resonant pulses.

[4]While in a typical MTsat experiment $\beta_{\text{ref}} = \beta_{\text{nom}}$, which would make the definition of β_{ref} redundant, below we experimentally vary β_{nom} and so the distinction between these two angles becomes important.

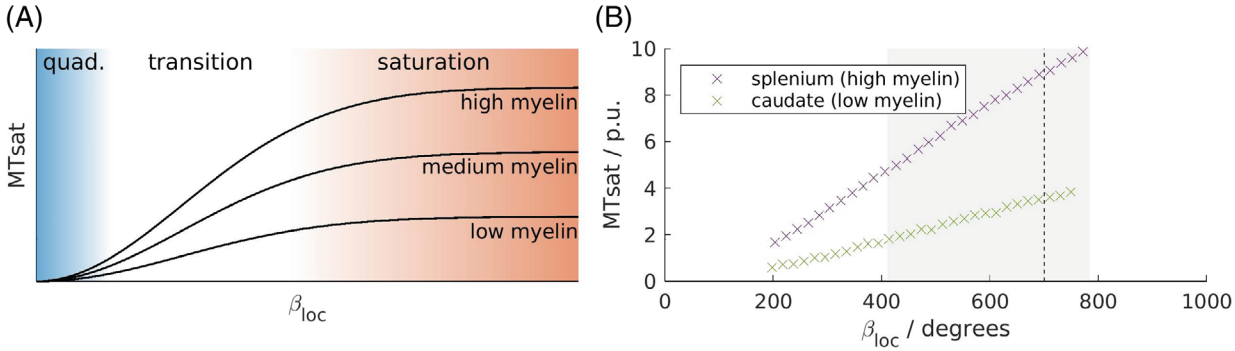

FIGURE 2 (A) Schematic representation of the β_{loc} dependence of magnetization transfer saturation (MTsat) for different myelination levels (black lines). Three regimes can be distinguished: a quadratic (quad.) scaling regime at low β_{loc} (blue), a transition region for intermediate β_{loc} (white), and the approach to full saturation of the macromolecular pool at high β_{loc} (red). MTsat values corresponding to anatomical regions with different myelination levels are represented by different multiplicative scalings of a universal function of β_{loc} ($\varphi(\beta_{loc})$; Equation 5). (B) The experimentally observed β_{loc} dependence of MTsat in single voxels in two distinct anatomical regions: the highly myelinated splenium of the corpus callosum (purple) showing higher values of MTsat and the low myelinated caudate nucleus (green) showing lower values of MTsat. The gray shaded area shows the range of β_{loc} values over the sample when $\beta_{nom} = \beta_{ref}$, the reference MT flip angle (here 700°), which is shown by the dashed line. MTsat shows an approximately linear increase with β_{loc} over this shaded area, suggesting that we are in the transition region. The previous B_1^+ correction (used for example in the hMRI toolbox[14]) applies below this range.[21,24] Note that the ability to distinguish these two areas increases with increasing β_{loc}. p.u., percent units

2.6 | Correction of MTsat maps using the linear model

Once the value of A has been determined in a calibration experiment it can be used to correct the bias in MTsat maps. By rearranging Equation (7) for MTsat(β_{ref}) we obtain the transformation of MTsat that corrects it from its value at β_{loc} to its value at β_{ref}:

$$\mathrm{MTsat}(\beta_{ref}) = \frac{\mathrm{MTsat}(\beta_{loc})}{1 + (\beta_{loc} - \beta_{ref})A}. \tag{8}$$

As in Reference 14, Equation (8) can be written in terms of a calibration parameter $C = \beta_{ref}A$:

$$\mathrm{MTsat}(\beta_{ref}) = \frac{\mathrm{MTsat}(\beta_{loc})}{1 + ([\beta_{loc}/\beta_{ref}] - 1)C}. \tag{9}$$

Using Equation (4) we can write $\beta_{loc}/\beta_{ref} = f_T\beta_{nom}/\beta_{ref}$ and so

$$\mathrm{MTsat}(\beta_{ref}) = \frac{\mathrm{MTsat}(\beta_{loc})}{1 + (rf_T - 1)C}, \tag{10}$$

where

$$r = \beta_{nom}/\beta_{ref}. \tag{11}$$

The general Equation (10) applies for any β_{nom} within the range of validity of the model. However, in the usual case where $\beta_{ref} = \beta_{nom}$ (i.e., we have chosen the reference flip angle for the parameter C estimation to be the nominal flip angle which we will use for future datasets), $r = 1$ and so Equation (10) simplifies to

$$\mathrm{MTsat}(\beta_{ref} = \beta_{nom}) = \frac{\mathrm{MTsat}(\beta_{loc} = f_T\beta_{nom})}{1 + (f_T - 1)C}. \tag{12}$$

For convenience in the following, we can write Equation (12) in terms of a local correction factor $F(f_T, C)$

$$\mathrm{MTsat}(\beta_{ref} = \beta_{nom}) = F(f_T, C)\mathrm{MTsat}(\beta_{loc} = f_T\beta_{nom}), \tag{13}$$

where

$$F(f_T, C) = \frac{1}{1 + (f_T - 1)C}. \tag{14}$$

In Equation (12) the utilized C can be the result of fitting to data from each voxel separately, to data aggregated across all voxels in a single brain or to data aggregated across several brains. Consequently, the correction can be applied with voxel-specific, individual-based global or group-based global parameters to obtain less precise but more robust corrections. Since a generalization of the correction is desirable, that is, a globally fixed parameter would be preferred, a comparison between these approaches is made below.

3 | METHODS

3.1 | Postmortem tissue specimens

Five whole postmortem chimpanzee brains (two females, aged from 12 to 43 years) were studied. These brains were acquired from wild and captive deceased chimpanzees who died unexpectedly of causes not related to this study (see Table S1 for more information). The general preparation of the tissue is described in References 30-32. postmortem interval before fixation varied from 1 to over 16 hours between brains (Table S1). Different ages and different postmortem intervals before fixation resulted in a broad variation of R1 (between 1.1 and 2.6 s^{-1}) and R2* (between 22 and 37 s^{-1}; Table S1). Thus our sample covers the broad variety of animal ages, tissue fixation conditions, and variation of tissue quality typically used in postmortem experiments on hominoid brains.

3.2 | Data acquisition setup

For MRI data acquisition, the brains were placed in a spherical acrylic container filled with perfluoropolyether (Fomblin). Constant temperature during the scanning (27.5–33.5°C) was facilitated by a warm air stream and monitored by a sensor (LUXTRON Corporation). See Supplementary Methods in Appendix S1 for more details.

3.3 | MRI acquisition

All data were acquired on a 7T whole-body MRI system (Terra 7T, Siemens Healthineers) equipped with a 1-channel transmit/32-channel receive RF head coil (Nova Medical).

3.3.1 | MPM protocol

An MPM protocol[14,15,33] was used (Figure 1) consisting of ultra-high resolution 3D FLASH images recorded with an isotropic resolution of 300 μm (matrix: $432 \times 378 \times 288$; readout bandwidth = 331 Hz/pixel; TR = 70 ms; 12 equidistant echoes (echo times [TE1, … ,TE12] = [3.63, … , 41.7] ms); excitation flip angles: $\alpha_{T1} = 84°$, $\alpha_{PD} = 18°$, $\alpha_{MT} = 18°$ for T1-, PD- and MT-weighted images, respectively). A Hann-filtered Gaussian-shaped MT saturation pulse at 3 kHz off-resonance with $\beta_{nom} = 700°$ and length 6 ms gave MT weighting. No partial k-space acceleration was employed.

3.3.2 | Calibration experiment

The calibration experiments were performed using an MPM protocol with similar imaging parameters, but at a lower isotropic resolution of 2.1 mm (matrix: $64 \times 56 \times 48$, bandwidth = 322 Hz/pixel, [TE1, … ,TE12] = [3.6, … , 41] ms) to accelerate the acquisitions.

T1-weighted and PD-weighted images were acquired once at the beginning of each session, followed by MT-weighted images with β_{nom} ranging from 220° to 760° (in two brains to 700° due to reaching hardware safety limits), in 20° intervals. The order of the different acquisitions was pseudo-randomized (see Supplementary methods in Appendix S1) to balance out potential drifts related to heating or scanner instabilities.

A brain mask was obtained for each brain through intensity thresholding of the first echo of the T1-weighted images.

3.3.3 | B_1^+ mapping

Maps of the RF transmit field B_1^+ were obtained using the method in References 28, 29 using a spin echo–stimulated echo 3D-echo-planar imaging sequence (4 mm isotropic resolution, matrix: $48 \times 64 \times 48$, TR = 500 ms, TE = 40.54 ms; mixing time = **34.91** ms; spin echo flip angles from 120°–330° in 15° increments; GRAPPA acceleration factor = 2×2) and B0 mapping using a gradient echo sequence (2 mm isotropic resolution, matrix: $96 \times 96 \times 64$, TR = 1020 ms, TE = 10 and **11.02** ms, excitation flip angle = 20°).

B_1^+ maps were computed with the hMRI toolbox.[14] A global reference T1 = 500 ms was used to account for T1 recovery during the mixing time between the spin echo and the stimulated echo.[29,34] B_1^+ maps were smoothed using Gaussian smoothing (8 mm median filter kernel) and then divided by a brain mask smoothed in the same way. B_1^+ maps were then upsampled to the respective resolution of the FLASH images using FSL `flirt` (using image header information only). f_T was determined by dividing the obtained relative B_1^+ map in p.u. by 100%. Note that by using smoothed, low-resolution maps of B_1^+ we interpolate across variations of B_1^+ on a smaller scale and capture only the large variation of the B_1^+ amplitude on the scale of the size of the brain with our correction.

3.4 | Preprocessing and MTsat calculation

MPM maps were computed separately for each nominal MT pulse flip angle (β_{nom}).

All weighted FLASH images were corrected for off-resonance-related distortions in the readout direction, which alternated between odd and even echoes due to the bipolar readout scheme. First the geometric mean of the first and third echo was calculated, which is an estimate of a virtual second echo image acquired with the opposite readout polarity.[35] Using the second acquired echo and the virtual echo as input, the HySCO algorithm of the ACID toolbox (http://diffusiontools.com/) was used to estimate the distortions and correct all acquired echoes.[36]

The effective transverse relaxation rate (R2*) was estimated using an ESTATICS[37] weighted log-linear least squares fit, as implemented in the hMRI toolbox.[14,38] No registration was performed between the weighted images. From this fit, the weighted images were extrapolated to TE = 0. These images were then used to calculate MTsat[13] using Equations (1), (2), and (3). In contrast to Reference 13, we used the local excitation flip angles in the calculation and not the nominal flip angles.

For the analysis with the low-resolution calibration data, we created binary masks excluding areas strongly affected by air bubbles. We did this by fitting a simple ordinary least squares model to describe the signal decay over the echos with an exponential function. Voxels in which the model explained less than 95% of the variance were excluded from the statistical analysis of the calibration data.

3.5 | Calibration parameter estimation and correction

For each voxel within the brain mask and each β_{nom} the local β_{loc} for the calibration experiment was calculated using Equation (4) and the experimental f_T map. The experimental dependence of MTsat on β_{loc} was fit voxel-wise using Equation (7) using nonlinear regression as implemented in MATLAB's `nlinfit`(R2021a). The fit parameters provide a voxel-wise estimation of the calibration parameter A in Equation (7). `nlinfit` also gave an estimate of the standard errors of the parameters. The parameter C in Equation (12) was obtained by multiplying by the nominal target flip angle β_{ref} (700° converted to radians). Similarly, the standard error of the fitted parameter C was obtained by multiplying the standard error of A by the nominal target flip angle β_{ref} (700° converted to radians) and converted to % units relative to the estimated$C$.

When the β_{loc} is too low, MTsat cannot be estimated reliably.[24] We therefore excluded data points with β_{loc} less than our lowest nominal flip angle (220°) from the fit. Low signal-to-noise ratio and artifacts can give rise to negative MTsat estimates; these data points were also excluded.

Descriptive statistics of C were calculated across all voxels in the brain mask. The mean of each calibration parameter across each specimen was used as an individual-based calibration parameter for this specimen. Then, the means of these individual-based parameters across all specimens were used as group-based calibration parameters (a group-based $C = 1.2$ for $\beta_{nom} = 700°$ was determined). Individual-based parameters were rounded to two decimal places before applying bias correction. Finally, two different corrections were applied to high-resolution MTsat maps, using the B_1^+ maps and the two different types of calibration parameters (individual-based vs. group-based).

4 | RESULTS

4.1 | The calibration coefficient C: estimation uncertainty, within- and between-brain variation

Examples of the MTsat dependence on β_{loc} obtained in the calibration experiment for individual voxels are shown in Figure 3. Plotted in normalized coordinates the dependencies measured for different voxels and different brains overlapped within experimental error, supporting the plausibility of our model assumption of a universal dependence of MTsat on β_{loc}. The dependence of MTsat on β_{loc} was very well described by the proposed linear model for all brains (Table 1, Figures 3 and 4) as reflected in the high goodness of fit, with the average (median) R^2 across the brain exceeding 0.95 in all five specimens (Table 1). The uncertainties of C estimated for each voxel and averaged across the brain lay between 0.6% and 1.1% of the mean value with the exception of brain 1 with an average uncertainty of 3.2% due to the scanner drift during the calibration experiment for this brain (Table 1, Figure 4). Larger errors in the estimation of C were observed at the edges of the brain (indicated by the large SD of the model fit in Figure 4) and around air bubbles within the sample, probably due to the low signal and the effect of mechanical and scanner drifts during the calibration experiment.

The means of the calibration coefficient C for the five brains were all close to 1.2 (varying between 1.18 and 1.24), with a mean of 1.209 and an SD of 0.026 between the brains corresponding to 2% of the mean C value. The histograms of C for the five brains showed unimodal overlapping distributions (Figure 3). The between-voxel variation

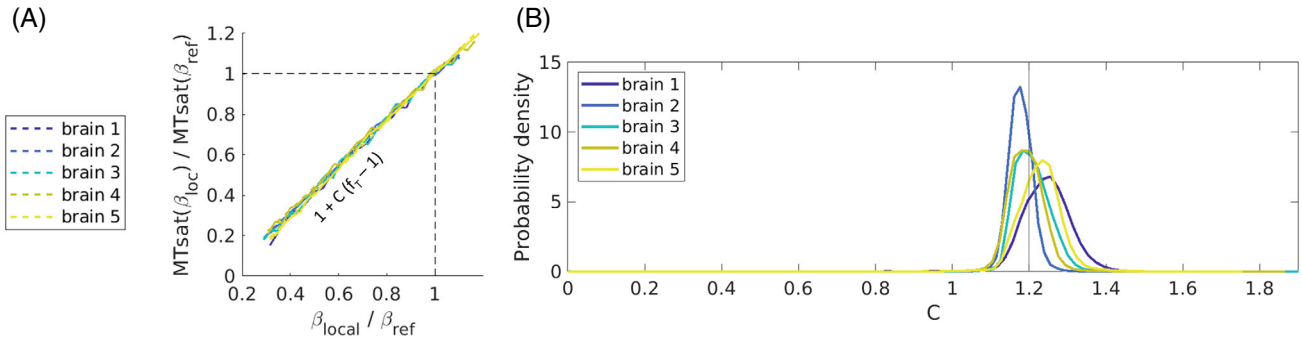

FIGURE 3 Distribution of the calibration parameter C. (A). Voxel-wise dependencies of magnetization transfer saturation (MTsat) on β_{loc} obtained in the calibration experiment for exemplary white matter voxels from five brains (solid lines) together with linear model fit (dashed lines). The dependencies are presented in the normalized coordinates MTsat(β_{loc})/MTsat(β_{ref}) and β_{loc}/β_{ref}. The linear model yielded high goodness of fit, providing voxel-wise estimation of C. In the normalized coordinates C corresponds to the slope of the fitted linear dependence. Note that experimental data from all brains nearly overlapped when plotted in normalized coordinates and are therefore described well by similar values of C. (B) Histograms for C across all voxels of each specimen. The histograms obtained for five brains overlapped and were centered around $C = 1.2$ (gray line), with some variation within and between the brains.

TABLE 1 Estimated values for the calibration parameter C and related variances

Brain	C	Between voxel variance of C (% from mean C)	Within-voxel uncertainty of C (% from fitted C)	Model fit	ρ_{part}(MTsat) C versus B_1^+	$\rho_{part}(B_1^+)$ C versus MTsat
Brain 1	1.242 ± 0.071	5.733	3.233 ± 23.160	0.952 ± 0.096	−0.124	−0.635
Brain 2	1.177 ± 0.030	2.567	0.643 ± 0.526	0.996 ± 0.013	−0.503	−0.534
Brain 3	1.207 ± 0.046	3.802	0.743 ± 0.978	0.993 ± 0.029	−0.390	−0.622
Brain 4	1.191 ± 0.047	3.951	1.149 ± 10.634	0.988 ± 0.042	−0.369	−0.574
Brain 5	1.227 ± 0.053	4.332	0.960 ± 1.841	0.990 ± 0.039	−0.312	−0.747

Notes: The mean, between-voxel variance and the within-voxel uncertainty of the estimated parameters C across all voxels for the five brains are provided. Voxels with values of $C < 0$ (assumption that only positive correlations are physical) or $C > 1.4$ (assumption that MTsat(β_{loc}) is positive for all β_{loc} down to 220° given $\beta_{ref} = 700°$; derived from Equation 10) were excluded from these statistics. Uncertainties and variance are provided in % from C. The within-voxel uncertainty was estimated from the SD of the fitted parameter and is reported in % from the fitted C. The between-voxel variance was estimated as the SD across the brain converted to % of mean C. The quality of the linear model fit (coefficient of determination R^2) is provided as mean ± SD across the brain. To quantify the dependence of the estimated C on the underlying B_1^+ and the corrected tissue MTsat, whole-brain voxel-wise partial Spearman correlation coefficients were calculated.

(standard deviation; SD) of C within each brain ranged from 2.6% to 5.7% of the mean value and exceeded the averaged within-voxel uncertainty of the C and between brain variation of C (Table 1).

That we obtained similar values of the calibration coefficient for brains with different ages and varying fixation conditions demonstrates the wide generalizability of the proposed calibration approach for postmortem brain imaging.

4.2 | Residual tissue-type dependence of C

A key assumption behind the applied approach was that C is independent of the macromolecular content and tissue type (Equation 5). This assumption was largely supported by the experimentally obtained values of C (Figure 3), which showed very close agreement across the brains and even between the brains with different fixation conditions and from individuals of different ages. However, the spatial distribution of C demonstrated residual systematic contrast between gray and white matter regions, with white matter showing on average 2.5% lower values of C as compared to gray matter (Figure 4). To illustrate the residual dependence of C on tissue type and underlying B_1^+, we computed the histograms of C within cortical and white matter voxels separately in one of the brains (Figure 5). These show different distributions of B_1^+ and C between cortex and white matter. Also, C showed small systematic differences between areas of low and high B_1^+. Figure 5B shows that the effects of B_1^+ and tissue type are partly

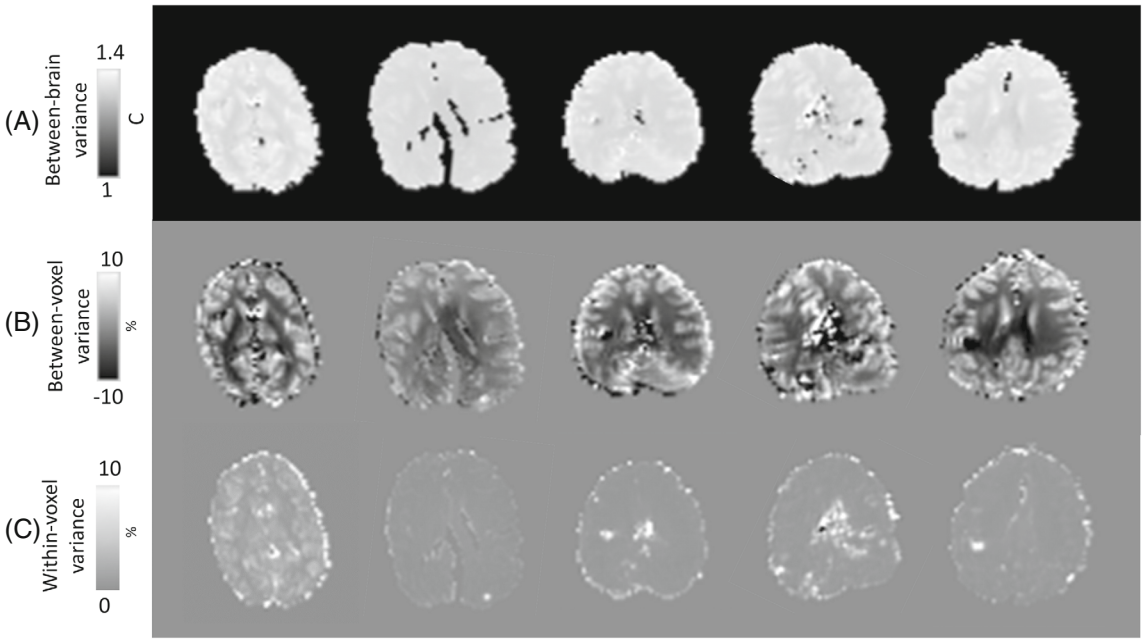

FIGURE 4 Variance of the calibration coefficient C. (A) Maps of calibration coefficient C for the five investigated brains obtained by a voxel-wise fit of the experimental dependence of MTsat on β_{loc}. All five brains demonstrated similar values of the calibration coefficient C all close to 1.2, with very low variation across the brain. (B) Between-voxel variance in C is illustrated through % difference from the mean value. (C) Maps of within-voxel uncertainty for C estimates, expressed in the parameter SD converted to % to C of that voxel

independent of each other, as the relationship between B_1^+ and C is clearly visible even if just white matter voxels are considered. Additional analysis of this residual dependence using Spearman correlation is presented in "Supplementary residual C dependence on tissue type and B_1^+" in the Appendix S1.

Next, we tested the practical relevance of this residual dependencies by comparing the bias correction with the voxel-wise versus average C values.

4.3 | Bias correction in MTsat maps: comparing calibration approaches

We tested the performance of the proposed calibration approach for the correction of the bias in MTsat maps resulting from the inhomogeneity of B_1^+. For each brain we corrected the bias in MTsat maps in three different ways, "voxel-wise," "individual-based," and "group-based." Voxel-wise refers to using each voxel's estimated C parameter, and individual-based refers to using the specific brain's median calibration parameter C (as reported in Table 1). Group-based refers to correcting with a fixed set of calibration parameters, i.e, the mean across all brains ($C = 1.2$).

Given the residual spatial dependence of C, in theory, corrections with voxel-wise C should provide most accurate results, while requiring a time-consuming calibration experiment which is only feasible for low-resolution MTsat maps, since repeating the whole calibration experiment for lengthy high resolution scans would require infeasibly long scanning times. Corrections with whole-brain values also requires a calibration experiment on each sample, but would be feasible for ultra-high resolution data by performing a calibration experiment at low resolution. Correction of group-based mean values is less accurate but most time efficient, since it requires a calibration experiment for only a subset of representative samples. In the following we evaluated the difference between these three proposed approaches.

4.3.1 | Voxel-based versus individual-based correction

Figure 6 shows the comparison between voxel-wise and individual-based correction in one exemplary brain. Visible reduction of the bias was achieved with both approaches, with the average difference between corrected maps lying within the ±0.5 p.u. interval.

To quantify the B_1^+ bias and the effect of the correction, spatial Spearman correlations were calculated between the apparent MTsat and B_1^+ across the brain. Due to field focussing in head-sized objects in ultra high field MRI, B_1^+ has a maximum at the center of the brain.[18,19] Therefore the B_1^+ distribution is spatially correlated with

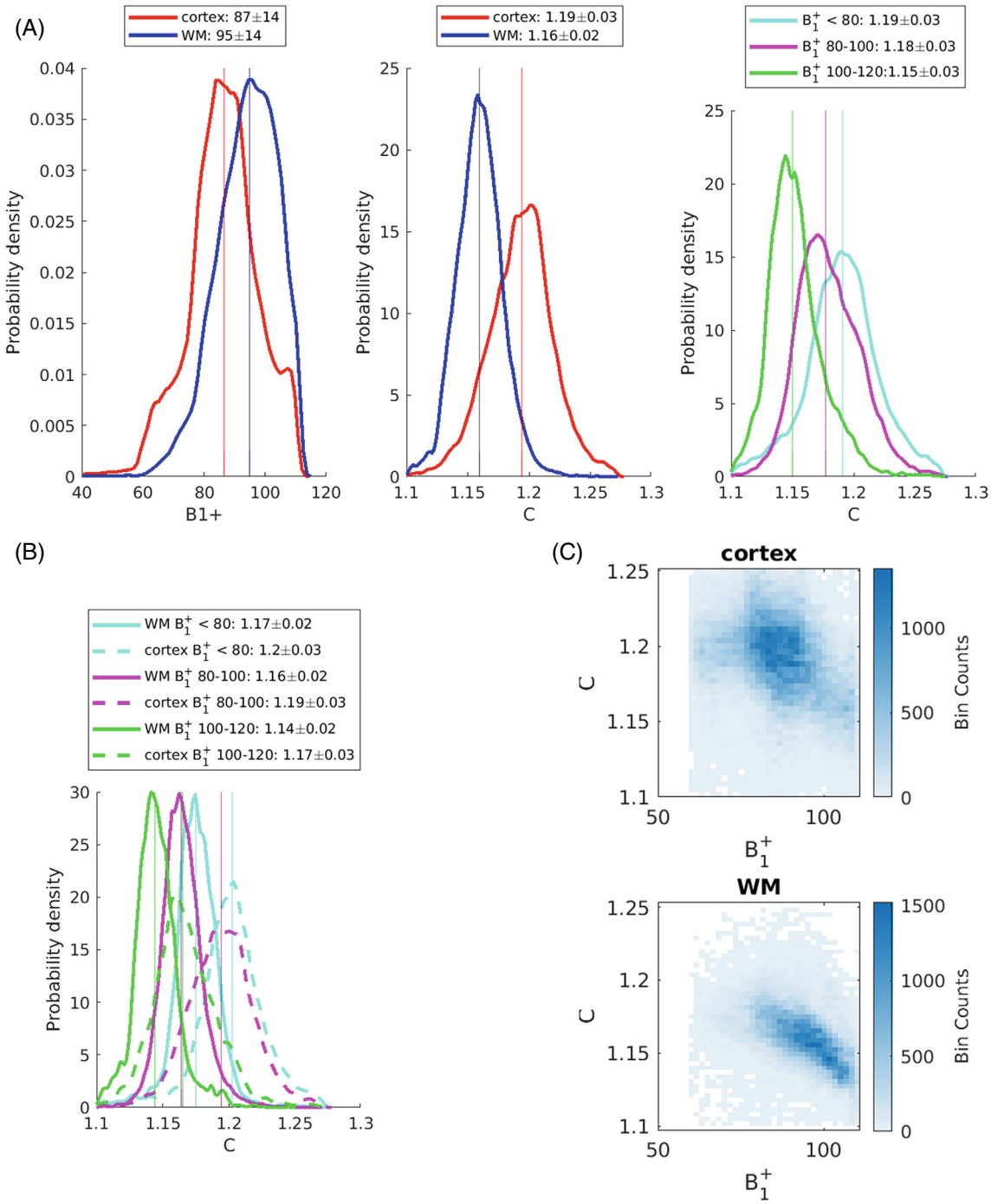

FIGURE 5 Effects of tissue type and B_1^+ on C in a representative brain (specimen 2). (A) Left: Histograms show lower values of B_1^+ in cortex than in white matter (WM). Middle: Parameter C is higher in cortical voxels than in WM voxels. Right: Distributions of C based on B_1^+, showing the lowest values of C in regions with the highest B_1^+. Both tissue type and B_1^+ independently explain variance in C across the brain, as quantified by partial correlation coefficients (Table 1). Median ± interquartile range are provided in the legend. (B) The interaction between tissue type and B_1^+. The effect of B_1^+ (denoted by different colors) can be seen for both tissue types (WM in solid line, cortex in dashed line). (C) The relationship between B_1^+ and C is additionally illustrated in density scatter plots for cortex and WM voxels separately. The relationship is particularly visible in the WM. Cortex and white matter masks were obtained using Freesurfer (https://surfer.nmr.mgh.harvard.edu/).

anatomy (white matter in the middle of the brain, gray matter in the periphery). We regressed out the effect of anatomy by using the B_1^+-independent measure R2* (Table S2). The correlation coefficients for uncorrected data ranged from $r = 0.422$ to $r = 0.633$. All three correction approaches were able to reduce that bias (reducing

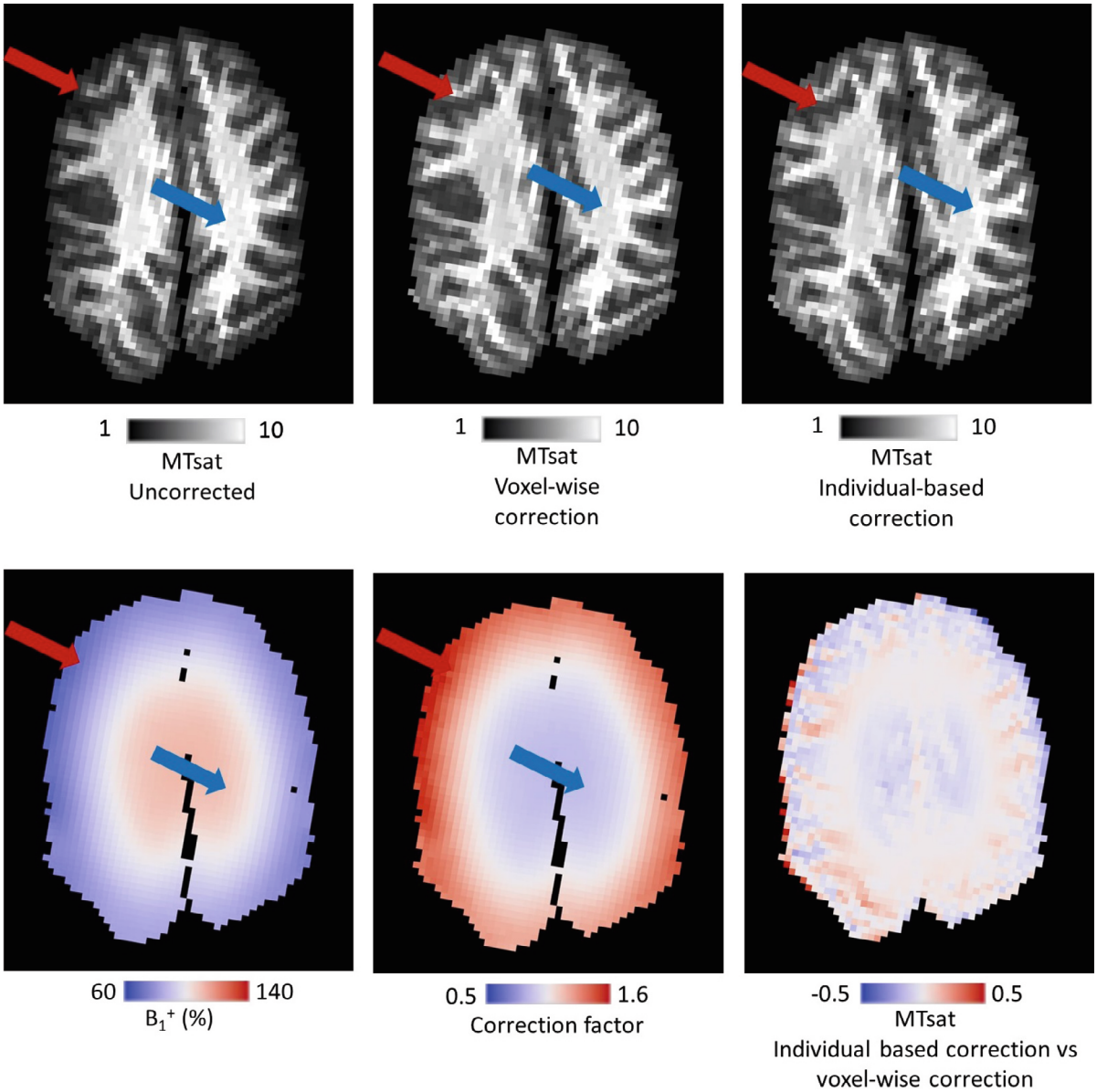

FIGURE 6 Example maps of MTsat. Top: Correction of the MTsat map. An axial slice of the uncorrected map is shown and compared to a voxel-wise correction and the individual-based correction approach. The red arrow indicates a region of low β_{loc}, whose hypointensity was corrected. The blue arrow indicates an area of high β_{loc}, whose hyperintensity was corrected. Bottom: The β_{loc} and corresponding correction factor (calculated using Equation 14, with either voxel-wise or individual-based mean C) are shown, along with the difference map between voxel-wise and individual-based correction. Tissue contrast and features of β_{loc} are visible in this map.

the correlations to between $r = -0.116$ and $r = 0.307$). The correction had an average effect on MTsat of 11%–16% of the uncorrected value, while the difference between correction approaches lay in the range of less than 0.5% (for all numbers see Table S2). Therefore, the observed variability in C across the brain is negligible compared to the B_1^+-bias in MTsat maps. Additionally, comparing the voxel-wise to the individual-based correction revealed some voxels with very large differences (indicated by the max values reported in Table S2) indicating that voxel-wise corrections fail in some regions prone to artifacts induced by either low signals or scanner instability during the calibration experiment, which can particularly affect brain edges.

4.3.2 | Individual-based versus group-based correction

For each brain we also B_1^+-bias corrected the ultra-high resolution MTsat maps in two different ways, "individual-based" and "group-based," as described above.

In the B_1^+-uncorrected data, partial correlation coefficients ranging from $\rho = 0.440$ to $\rho = 0.589$ were observed, reflecting the B_1^+-induced bias in MTsat. The relationship between B_1^+ and MTsat was lower for all corrected data sets and ranged from $\rho = -0.094$ to $\rho = 0.196$ with the individual-based correction and from $\rho = -0.077$ to $\rho = 0.201$ with the group-based correction. We also quantified the effect of the applied corrections on the MTsat values. Across all voxels, the average effect of applying the correction was an absolute change between 11.75% and 18.90% in MTsat (Table S3). Comparing the two correction approaches to each other, the individually and group-based corrected MTsat maps differed on average by 0.14%–0.42%.

Figure 7A,B illustrates that bias correction of the MTsat values across the brain visibly reduces the bias and yields more distinct histogram peaks of gray and white matter. Figure 7C shows that uncorrected cortical surface MTsat maps strongly resemble the B_1^+ distribution. After correction the maps show patterns reflecting myeloarchitecture, with the highly myelinated primary cortical areas standing out. For example, the expected high myelination of primary motor and primary somatosensory cortex along the central gyrus only becomes apparent after the correction. This demonstrates that bias correction in MTsat maps is a crucial step when studying cortical myelination across the entire brain and enables quantitative comparison of myelination between cortical areas.

5 | DISCUSSION

We have developed a calibration correcting for B_1^+-induced biases in MTsat maps and demonstrated its efficacy. It extends previous calibration approaches to the higher 7T static magnetic field strength and the stronger MT saturation pulses used for postmortem imaging. A high goodness of fit of the calibration model to experimental data

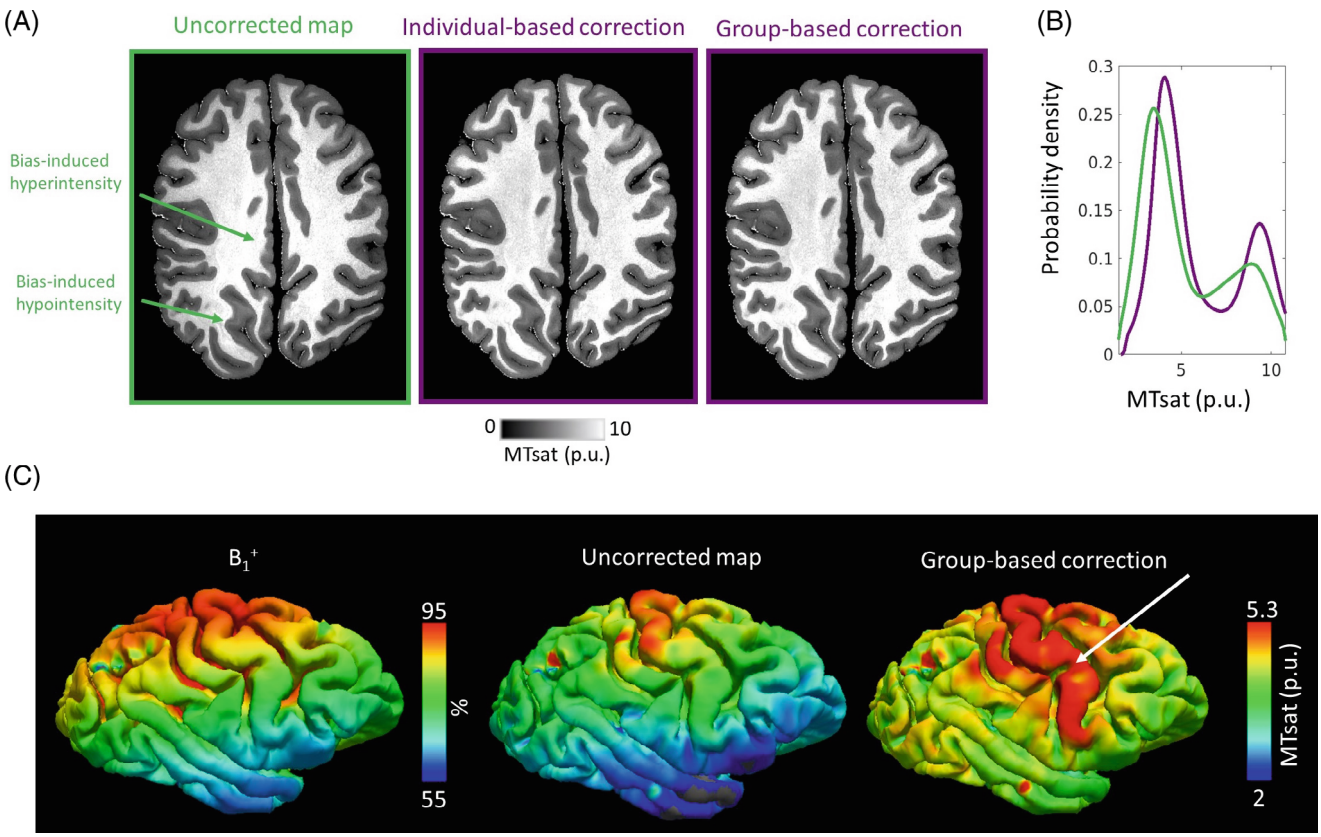

FIGURE 7 Correction of high-resolution images. (A) The effect of B_1^+ bias correction on an example high resolution MTsat axial slice from brain 2. (B) A histogram comparing the distribution of the uncorrected map (green) to correction with the individual-based parameters and group-based parameters (purple). The corrected maps show an emphasized bimodal distribution of values, reflecting gray and white matter, while the uncorrected map provides a poorer distinction. The bias visible in the uncorrected map is reduced in both corrected maps. The probability density plot was created with the MATLAB function `ksdensity` using 100 bins and excluding outliers (data points below the second or above the 98th percentile). (C) The distribution of B_1^+ (left) on the Freesurfer (https://surfer.nmr.mgh.harvard.edu/) mid-cortical surface of brain 2 is shown, demonstrating that B_1^+ can also systematically vary across cortical regions. If not corrected, this is also reflected in the cortical MTsat maps (middle). Our correction eliminates this bias, revealing the highly myelinated primary cortical areas (right; arrow).

supports the theory-based correction approach. Although the status and quality of the tissue varied significantly, we found a single fixed calibration parameter that significantly reduced the B_1^+-induced bias in all postmortem data sets, corroborating the generalizability. This simplifies the implementation as a standard tool, since calibration parameters do not need to be estimated for each postmortem specimen individually, which would require the acquisition of additional reference data for each specimen.

5.1 | Factors influencing the estimation of *C*

The presented calibration requires the experimental estimation of the calibration parameter C. A strong overall goodness of fit suggests the validity of the theoretical model. The R^2 of >0.95 we obtained for all brains vastly exceeds the average R^2 of 0.20 that was reported in a similar experiment conducted on humans in vivo, in which the model was fit over large regions which were assumed to be homogeneous.[24] Here, we fit the model and estimate C voxel-by-voxel, which, unlike region-based analyses, captures spatial inhomogeneities of the calibration curve. However, voxel-wise estimations are more sensitive to variations in statistical noise, B_1^+ errors and the underlying tissue. This limitation is lifted by using whole brain average or group averaged calibration coefficients.

The use of a global C was based on an assumption that C does not depend on B_1^+ amplitude, tissue characteristics or tissue type. In our data, the calibration parameters systematically differed between gray and white matter by about 4% (also apparent in a significant spatial correlation between C with the corrected MTsat values). This indicates that using different values of C for gray and white matter may provide better correction. Note that in the one brain where we analyzed the calibration coefficient C separately in gray and white matter the global calibration coefficient C was closer to the maximum of the distribution of fitted C values for gray matter voxels than to the white matter maximum. One reason for this may be the fact that gray matter is located on the periphery of the brain, in regions with low B_1^+ and therefore requires stronger correction. Also some residual dependence on B_1^+ was observed. Higher local B_1^+ is expected in regions of higher conductivity but can only be observed using high-resolution B_1^+-mapping, for example, by MP3RAGE.[39] We calculated global, individual-based calibration parameters for each brain by taking the mean values across all voxels. Corrections using voxel-wise values of C did not result in a better correction than using brain-averaged values of C (Table S2), so this residual tissue and B_1^+ dependence has a negligible effect on correction performance.

5.2 | Consistency of *C* across brains

Overall, the variability of the estimated calibration parameters within individual brains (Table 1) was larger than variability between brains. This indicates that factors such as tissue quality, postmortem time etc. play only a minor role and a generalized correction is possible. Correction using the group-based mean calibration parameters of our sample ($C = 1.2$) visibly reduced the bias in all brains. Individually optimising the calibration coefficients may yield more accurate correction results. However, when comparing the individually and group-based corrected maps, average differences of less than 0.5% were obtained. In comparison to the average 12%–19% change that either correction had on the uncorrected maps, this appears minor. Therefore, a correction with the group-based parameters is recommended when individual-based parameters are not available, that is, when additional reference data are not available.

For data obtained postmortem at 7T with the acquisition parameters used in our study, the following equation with group-based $C = 1.2$ can be applied for correction:

$$\mathrm{MTsat}(\beta_{\mathrm{ref}} = 700°) = \mathrm{MTsat}(\beta_{\mathrm{loc}} = f_{\mathrm{T}} \cdot 700°)\frac{1}{1+1.2(f_{\mathrm{T}}-1)}. \tag{15}$$

5.3 | Correction approach reveals true biological variability

As a ground-truth for MTsat is generally not available, we assessed the performance of the B_1^+-bias correction by directly comparing the different types of corrections with respect to their anatomical validity. All correction approaches had a significant impact on MTsat values, with an average change of up to 20% of the uncorrected value. The two separate gray and white matter peaks in whole sample MTsat histograms became better separated after correction (Figure 7). This indicates that nonbiological sources of variance were being reduced. Additionally, cortical surface projections of uncorrected MTsat maps lead to visible biases that correspond to the B_1^+ distribution across the cortex (Figure 7). Visual assessment of corrected and original uncorrected MTsat maps showed reduced bias and clearer delineation of anatomical structures (e.g. motor and somatosensory cortex; Figure 7).

5.4 | Previous approaches

We used an empirical approach to determine a functional form for the correction of B_1^+ bias. The functional form could alternatively be elucidated by using forward models of the MT effect to simulate the dependence of MTsat on β_{loc} and m.[22] However this method is limited by the need for reliable forward model parameter estimates (exchange times, pool size ranges and relaxation times/lineshapes of the macromolecular and free pools). These are sensitive to tissue preparation methods, difficult to measure, and not generally available.

Comparison of the correction method presented here to the previous in vivo correction method used in References 21,23,24 can be found in the subsection "Comparison with the previous calibration model" in Appendix S1.

5.5 | Limitation: potential acquisition protocol dependence

Although a linear dependence on the flip angle is expected in the transition region, this specific calibration approach was only tested on one hardware setup and protocol. We show in Appendix S1 how Equation (15) can be modified (see Equations (S.1) and (S.2)) to map the measured MTsat to different β_{ref} flip angles within the region where the linear model applies.

The value of the global calibration coefficient ($C = 1.2$) reported in this study was obtained for formalin-fixed chimpanzee brains at 7T using a specific MPM protocol and MT saturation pulse. This could potentially limit general applicability of this specific C coefficient to other MT protocols. However, we note that C is a normalized estimate of the slope of MTsat with respect to β_{nom}. This normalization can be seen clearly in the case of a two point estimate of C from MTsat measured at two distinct MT pulse flip angles β_1 and β_1,

$$C = \frac{\text{MTsat}(\beta_2) - \text{MTsat}(\beta_1)}{\beta_2 - \beta_1} \frac{\beta_{\text{ref}}}{\text{MTsat}(\beta_{\text{ref}})}, \qquad (16)$$

where the first product term is the estimate of the slope and the second corresponds to the effective normalization: the numerator is the scaling between A and C (i.e., $C = \beta_{\text{ref}}A$) and the denominator corresponds to the factorization of the slope into a product with $\text{MTsat}(\beta_{\text{ref}})$ (see Equation 7). Such a normalized parameter will tend to be reasonably robust to small changes in the protocol and flip angles, as changes in the respective numerators and denominators will tend to cancel each other out. Therefore we expect that similar calibration coefficients will be obtained for different experimental implementations (e.g., for different MR system vendors).

However, if data are obtained with major changes in the acquisition protocol (e.g., β_{nom} far outside the experimental range used in the calibration), then recalibration may be required using the described calibration experiment. The calibration experiment is generally applicable to the broad range of potential experimental settings and estimation of C can be easily performed on a small number of postmortem specimens. The resulting group-based calibration parameters can then be used to correct all additional specimens. Future research may investigate which sequence parameters have no or little impact on the calibration parameters.

6 | CONCLUSION

We developed a B_1^+ correction of MT saturation (MTsat) maps using a calibration approach. It extends previous calibration approaches and enables quantitative postmortem MT mapping using high power MT saturation pulses at 7T. We showed that a single correction coefficient can visibly reduce B_1^+-related biases in low resolution data, high-resolution data and on cortical myelination maps.

ACKNOWLEDGMENTS

This project has been funded by the Max Planck Society and by the European Research Council under the European Union's Seventh Framework Programme (FP7/2007-2013) / ERC grant agreement number 616905. Nikolaus Weiskopf received funding from the European Union's Horizon 2020 research and innovation programme under the grant agreement number 681094. This project received funding from the Deutsche Forschungsgemeinschaft (DFG, German Research Foundation)—project no. 347592254 (WE 5046/4-2 and KI 1337/2-2). Gunther Helms was funded in part by the Swedish Research Council, grant NT 2014-6193. IL has been funded by the Deutsche Forschungsgemeinschaft (DFG, German Research Foundation)—project number 446291874. We are grateful to Caroline Jantzen, Felix Büttner, Niklas Alsleben and Franziska Zahn for their help with sample preparation and scanning. IL is grateful to Dr Daniele Agostini for help with debugging. Nikolaus Weiskopf and Gunther Helms contributed equally to this work. The EBC (Evolution of Brain Connectivity) consortium: Catherine Crockford (Institute of Cognitive Sciences, CNRS, Lyon, France), Roman Wittig (Institute of Cognitive Sciences, CNRS, Lyon, France), Anna Jauch (Max Planck Institute for Human Cognitive and Brain Sciences, Leipzig, Germany), Bala Amarasekaran (Tacugama Chimpanzee Sanctuary, Freetown, Sierra Leone), Carol

Asiimwe (Budongo Conservation Field Station, Uganda), Jenny E. Jaffe (Project Group Epidemiology of Highly Pathogenic Microorganisms, Robert Koch Institute, Berlin, Germany; Taï Chimpanzee Project, Centre Suisse de Recherches Scientifiques, Abidjan, Côte d'Ivoire), Fabian Leendertz (Epidemiology of highly pathogenic microorganisms, Robert Koch-Institute, Berlin, Germany; Helmholtz Institute for One Health, Greifswald, Germany; Tai Chimpanzee Project, CSRS, Abidjan, Ivory Coast), Matyas Liptovszky (Twycross Zoo, UK), Sophie Moittie (Twycross Zoo, UK), and Andrea Pizarro (Tacugama Chimpanzee Sanctuary, Freetown, Sierra Leone). Open Access funding enabled and organized by Projekt DEAL.

CONFLICT OF INTEREST

The Max Planck Institute for Human Cognitive and Brain Sciences has an institutional research agreement with Siemens Healthcare. NW holds a patent on acquisition of MRI data during spoiler gradients (US 10401453 B2). NW was a speaker at an event organized by Siemens Healthcare and was reimbursed for the travel expenses.

DATA AVAILABILITY STATEMENT

The analysis code can be found at https://github.com/IlonaLipp/MTcalibration. Data associated with this manuscript can be found at https://doi.org/10.17617/3.803OMM.

ORCID

Ilona Lipp https://orcid.org/0000-0002-5644-2057
Evgeniya Kirilina https://orcid.org/0000-0003-1304-4363
Kerrin J. Pine https://orcid.org/0000-0002-2486-2970
Gunther Helms https://orcid.org/0000-0002-1371-5123

TWITTER

Ilona Lipp @ilona_lipp

REFERENCES

1. Weiskopf N, Edwards L, Helms G, Mohammadi S, Kirilina E. Quantitative magnetic resonance imaging of brain anatomy: towards in-vivo histology. *Nature Rev Phys*. 2021;3:570-588.
2. Natu VS, Gomez J, Barnett M, et al. Apparent thinning of human visual cortex during childhood is associated with myelination. *Proc Nat Acad Sci*. 2019;116:20750-20759.
3. Edwards LJ, Kirilina E, Mohammadai S, Weiskopf N, Microstructural imaging of human neocortex in vivo. *NeuroImage*. 2018;182:184-206.
4. Paquola C, Bethlehem RA, Seidlitz J, et al. Shifts in myeloarchitecture characterise adolescent development of cortical gradients. *eLife*. 2019;8:e50482.
5. Whitaker KJ, Vértes PE, Romero-Garcia R, et al. Adolescence is associated with genomically patterned consolidation of the hubs of the human brain connectome. *PNAS*. 2016;113:9105-9110.
6. Möller HE, Bossoni L, Connor JR, et al. Iron, myelin, and the brain: neuroimaging meets neurobiology. *Trends Neurosci*. 2019;42:384-401.
7. Alkemade A, Bazin PL, Balesar R, et al. 7 Tesla MRI followed by histological 3D reconstructions in whole-brain specimens. *Front Neuroanat*. 2020;14:536838.
8. Kirilina E, Helbling S, Morawski M, et al. Superficial white matter imaging: contrast mechanisms and whole-brain in vivo mapping. *Sci Adv*. 2020;6:eaaz9281.
9. Henkelman RM, Huang X, Xiang QS, Stanisz GJ, Swanson SD, Bronskill MJ. Quantitative interpretation of magnetization transfer. *Magn Reson Med*. 1993;29:759-766.
10. Sled JG. Modelling and interpretation of magnetization transfer imaging in the brain. *NeuroImage*. 2018;182:128-135.
11. Helms G, Piringer A. Simultaneous measurement of saturation and relaxation in human brain by repetitive magnetization transfer pulses. *NMR Biomed*. 2005;18:44-50.
12. Tofts PS, Steens SCA, Buchem MA. Ch. 8. MT: magnetization transfer. In: Tofts P, ed. *Quantitative MRI of the Brain*. John Wiley & Sons, Ltd; 2004:257-298.
13. Helms G, Dathe H, Kallenberg K, Dechent P. High-resolution maps of magnetization transfer with inherent correction for RF inhomogeneity and T1 relaxation obtained from 3D FLASH MRI. *Magn Reson Med*. 2008;60:1396-1407.
14. Tabelow K, Balteau E, Ashburner J, et al. hMRI – A toolbox for quantitative MRI in neuroscience and clinical research. *NeuroImage*. 2019;194:191-210.
15. Weiskopf N, Suckling J, Williams G, Correia Marta M, Inkster B. Quantitative multi-parameter mapping of R1, PD*, MT, and R2* at 3T: a multi-center validation. *Front Neurosci*. 2013;7:95.
16. Leutritz T, Samson RS, Curt A, Helms G, Freund P, Weiskopf N. Multiparameter mapping of relaxation (R1, R2*), proton density and magnetization transfer saturation at 3T: a multicenter dual-vendor reproducibility and repeatability study. *Human Brain Mapping*. 2020;41:4232-4247.
17. Leitão D, Tomi-Tricot R, Bridgen P, et al. Parallel transmit pulse design for saturation homogeneity (PUSH) for magnetization transfer imaging at 7T. *Magn Reson Med*. 2022;88:180-194.
18. Hoult DI. Sensitivity and power deposition in a high-field imaging experiment. *J Magn Reson Imaging* 2000;12:46-67.
19. Collins CM, Liu W, Schreiber W, Yang QX, Smith MB. Central brightening due to constructive interference with, without, and despite dielectric resonance. *J Magn Reson Imaging*. 2005;21:192-196.
20. Volz S, Nöth U, Rotarska-Jagiela A, Deichmann R. A fast B1-mapping method for the correction and normalization of magnetization transfer ratio maps at 3 T. *NeuroImage*. 2010;49:3015-3026.
21. Helms G, Weiskopf N, Lutti A. Correction of FLASH-based MT saturation in human brain for residual bias of B1-inhomogeneity at 3T arXiv preprint arXiv:2104.14878, 2021.
22. Rowley CD, Campbell JS, Wu Z, et al. A model-based framework for correcting inhomogeneity effects in magnetization transfer saturation and inhomogeneous magnetization transfer saturation maps. *Magn Reson Med*. 2021;86:2192-2207.
23. Helms G. Correction for residual effects of B1+ inhomogeniety on MT saturation in FLASH-based multi-parameter mapping of the brain. *Proc Intl Soc Mag Reson Med*. 2015;23:3360.
24. Olsson H, Andersen M, Wirestam R, Helms G. Mapping magnetization transfer saturation (MTsat) in human brain at 7T:

protocol optimization under specific absorption rate constraints. *Magn Reson Med*. 2021;86:2562-2576.
25. Georgiadis M, Schroeter A, Gao Z, et al. Nanostructure-specific X-ray tomography reveals myelin levels, integrity and axon orientations in mouse and human nervous tissue. *Nature Commun*. 2021;12:2941.
26. Helms G, Dathe H, Dechent P. Modeling the influence of TR and excitation flip angle on the magnetization transfer ratio (MTR) in human brain obtained from 3D spoiled gradient echo MRI. *Magn Reson Med*. 2010;64:177-185.
27. Dathe H, Helms G. Exact algebraization of the signal equation of spoiled gradient echo MRI. *Phys Med Biol*. 2010;55:4231-4245.
28. Lutti A, Hutton C, Finsterbusch J, Helms G, Weiskopf N. Optimization and validation of methods for mapping of the radiofrequency transmit field at 3T. *Magn Reson Med*. 2010;64:229-238.
29. Lutti A, Stadler J, Josephs O, et al. Robust and fast whole brain mapping of the RF transmit field B1 at 7T. *PLoS One*. 2012;7:e32379.
30. Gräßle T, Crockford C, Eichner C, et al. Sourcing high tissue quality brains from deceased wild primates with known socio-ecology. *Methods Ecol Evol*. 2022; In press.
31. Eichner C, Paquette M, Mildner T, et al. Increased sensitivity and signal-to-noise ratio in diffusion-weighted MRI using multi-echo acquisitions. *NeuroImage*. 2020;221:117172.
32. Weiskopf N, Lutti A, Helms G, Novak M, Ashburner J, Hutton C. Unified segmentation based correction of R1 brain maps for RF transmit field inhomogeneities (UNICORT). *NeuroImage*. 2011;54:2116-2124.
33. Jiru F, Klose U. Fast 3D radiofrequency field mapping using echo-planar imaging. *Magn Reson Med*. 2006;56:1375-1379.
34. Weiskopf N, Klose U, Birbaumer N, Mathiak K. Single-shot compensation of image distortions and BOLD contrast optimization using multi-echo EPI for real-time fMRI. *NeuroImage*. 2005;24:1068-1079.
35. Ruthotto L, Kugel H, Olesch J, et al. Diffeomorphic susceptibility artifact correction of diffusion-weighted magnetic resonance images. *Phys Med Biol*. 2012;57:5715-5731.
36. Weiskopf N, Callaghan MF, Josephs O, Lutti A, Mohammadi S. Estimating the apparent transverse relaxation time (R2*) from images with different contrasts (ESTATICS) reduces motion artifacts. *Front Neurosci*. 2014;8:278.
37. Edwards LJ, Mohammadi S, Pine KJ, Callaghan MF, Weiskopf N. Robust and efficient R2* estimation in human brain using log-linear weighted least squares. *Proc Int Soc Magn Reson Med*. 2022;30:1264.
38. Olsson H, Andersen M, Kadhim M, Helms G. MP3RAGE: simultaneous mapping of T_1 and B_1^+ in human brain at 7T. *Magn Reson Med*. 2022;87:2637-2649.

SUPPORTING INFORMATION

Additional supporting information may be found in the online version of the article at the publisher's website.

Appendix S1. Supporting information

How to cite this article: Lipp I, Kirilina E, Edwards LJ, et al. B_1^+-correction of magnetization transfer saturation maps optimized for 7T postmortem MRI of the brain. *Magn Reson Med*. 2023;89:1385-1400. doi: 10.1002/mrm.29524